
Validation of patient-specific cerebral blood flow simulation using transcranial Doppler measurements

Derek Groen^{1,*}, Robin A. Richardson², Rachel Coy³, Ulf D. Schiller^{4,5}, Hoskote Chandrashekar⁶, Fergus Robertson⁶ and Peter V. Coveney^{2,3}

¹*Department of Computer Science, Brunel University London, London, United Kingdom*

²*Centre for Computational Science, University College London, London, United Kingdom*

³*Centre for Mathematics and Physics in the Life Sciences and Experimental Biology, London, University College London, London, United Kingdom*

⁴*Department of Materials Science and Engineering, Clemson University, Clemson, SC, USA*

⁵*School of Health Research, Clemson University, Clemson, SC, USA*

⁶*Lysholm Department of Neuroradiology, National Hospital for Neurology and Neurosurgery, University College London, London, United Kingdom*

Correspondence*:

Corresponding Author

Derek.Groen@brunel.ac.uk

2 ABSTRACT

3 We present a validation study comparing results from a patient-specific lattice-Boltzmann
4 simulation to transcranial Doppler (TCD) velocity measurements in four different planes of the
5 middle cerebral artery (MCA). As part of the study, we compared simulations using a Newtonian
6 and a Carreau-Yasuda rheology model. We also investigated the viability of using downscaled
7 velocities to reduce the required resolution. Simulations with unscaled velocities predict the
8 maximum flow velocity with an error of less than 9%, independent of the rheology model chosen.
9 The accuracy of the simulation predictions worsens considerably when simulations are run at
10 reduced velocity, as is for example the case when inflow velocities from healthy individuals are
11 used on a vascular model of a stroke patient. Our results demonstrate the importance of using
12 directly measured and patient-specific inflow velocities when simulating blood flow in MCAs. We
13 conclude that localized TCD measurements together with predictive simulations can be used to
14 obtain flow estimates with high fidelity over a larger region, and reduce the need for more invasive
15 flow measurement procedures.

16 **Keywords:** lattice-boltzmann, middle cerebral artery, computational fluid dynamics, transcranial doppler, high performance
17 computing, blood flow, validation study

1 INTRODUCTION

18 Computational fluid dynamics (CFD) has been widely applied by researchers to model blood flow in
19 cerebral arteries and specifically within aneurysms (1, 2, 3, 4, 5) . There is considerable interest in
20 exploring the correlation between the dynamical properties of blood flow and clinical outcomes, with the
21 long-term aim to provide a personalized, predictive simulation approach for aneurysm formation, growth
22 and/or rupture (6, 7, 8). When performing such simulations it is essential that computational models are
23 able to deliver a realistic prediction of patient-specific flow velocities.

24 A range of simulation studies have been performed using patient-specific flow measurements derived
25 from phase contrast magnetic resonance angiography (pc-MRA, see e.g. (9)). However, Marzo et al. (10)
26 found that using this type of measurement provides limited accuracy benefits in comparison with modelled
27 boundary conditions. The use of CFD in combination with transcranial Doppler (TCD) velocity measure-
28 ments has been less extensively researched (see e.g. Hassan et al. (11)), primarily because reliable TCD
29 measurements can only be made in a limited subset of the cerebral arteries. In addition, TCD measure-
30 ments with hand-held devices may contain errors if held at an incorrect angle (e.g., an underprediction
31 of approximately 1.6% if the angle is off by 10 degrees). However, the excellent time resolution of TCD
32 allows for a more reliable detection of peak velocities, and helps to establish more precise pulsatile flow
33 profiles. Indeed, the maximum velocity values found by TCD are frequently around 30% higher than those
34 found through pc-MRA (12, 13). In addition, TCD is non-invasive, unlike pc-MRA, and both are widely
35 applied in clinical settings today.

36 Blood consists of blood cells which reside within a liquid medium known as blood plasma. Blood has
37 a viscosity which decreases under shear flow (shear-thinning), unlike water which exhibits a constant
38 Newtonian viscosity regardless of shear strain rate. Many well-known CFD studies of cerebrovascular
39 blood flow are performed using a Newtonian fluid model (e.g. (5, 1, 2)), though recent research has found
40 that such an assumption could lead to over-estimation of wall shear stresses (WSS) in cerebral arteries and
41 aneurysms (14, 15, 16). As a result, it can also alter the outcome of related diagnostic techniques such
42 as three-band diagram analysis (7), a technique proposed by Chatzizisis et al. (17) to compare WSS at a
43 specific location, over a period of time, to a set of pathological threshold values.

44 Existing CFD studies of cerebrovascular flow frequently derive inflow velocities not from the specific
45 patient of interest, but from healthy subjects (e.g. (1, 2)) or idealized pulsatile profiles (Womersley flow,
46 e.g. (5, 18, 19)). However, blood flow velocities in middle cerebral arteries (MCA) from healthy subjects
47 are typically much lower than those from stroke patients or patients suffering from hypertension. In this
48 context Venugopal et al. (20) found that mean WSS properties of simulations at Reynolds numbers (Re)
49 below 200 do not correspond in any linear way to WSS properties of simulations at $Re=340-675$. Itani et al.
50 (21) investigated how the mean, maximum and minimum wall shear stress change when a patient is subject
51 to different levels of exercise intensity. They also found a non-linear relation between maximum inflow
52 velocity and extracted WSS.

53 In this work, we simulate blood flow in a patient-specific MCA model using patient-specific TCD
54 measurements as inflow boundary conditions, and compare our predictions against clinical measurements at
55 four locations. Our simulations employ the lattice-Boltzmann method at high resolution, a technique which
56 has been shown by Jain et al., among others, to be particularly well suited for simulating cerebrovascular
57 and aneurysmal blood flow (22). We perform simulations imposing the measured velocity from the
58 individual patients at the inlet, and investigate how the choice of rheology model affects the predicted flow
59 velocities throughout the MCA. In addition, we report on the accuracy of velocity predictions when running

60 simulations with downscaled inlet velocity, and rescaling the velocities obtained from the measurement
61 planes.

2 MATERIALS AND METHODS

62 To perform our simulations, we use the HemeLB software (23, 24) for lattice Boltzmann simulations
63 of blood flow in cerebral arteries. The lattice Boltzmann method (LBM) is a highly scalable simulation
64 approach which uses a discretized kinetic model on a regular lattice to reproduce the dynamics of incom-
65 pressible fluid flow. The LBM can be interpreted as a numerical solver for the Navier-Stokes equation with
66 the advantage that it algorithmically separates the non-linearity from the non-locality. Specific *boundary*
67 *conditions* are applied to create accurate representations of fluid flow near vessel walls, as well as inflow
68 and outflow boundaries. In our case, we adopt a 3-dimensional LBM which propagates fluid flow in
69 19 directions per grid point (D3Q19) using a BGK collision operator (see e.g. (25) for details). For the
70 boundary conditions, we used the Bouzidi (26) model to represent flow interactions with the vessel walls.
71 Patient-specific inflow conditions were obtained from TCD measurements performed at the National
72 Hospital for Neurology and Neurosurgery (NHNN) using the Doppler BoxX (with a handheld device)
73 from the DWL company, and used rotational angiography data from NHNN to obtain imaging data from
74 the same patient. TCD measurements were recorded for at least six cardiac cycles each in the right MCA,
75 consecutively at depths of 49, 54, 57, 59 and 63 mm away from the temple area (see Fig. 1 for the location
76 of the TCD validation planes in the 3D model, Table 2 for the velocity measurements, and Fig. 2 for the
77 TCD image measurement at the inflow boundary). The Doppler BoxX provides a flow direction indication
78 at all depths whenever a measurement is made. In our case, this feature enabled us to hold the TCD device
79 such that the flow was observable in the right MCA, as well as the right Anterior Communicating Artery
80 (ACA). This is important, because retaining such a tight orientation minimizes TCD measurement errors
81 caused by holding the device at a wrong angle. In addition, to align the TCD measurements precisely with
82 the corresponding planes of flow direction in the simulation domain, we performed a triangulation and an
83 angle correction with respect to the perpendicular flow direction (see Tab. 1 for our triangulation results).
84 The maximum velocity at the inflow boundary, extracted from the TCD data, was 1.50 m/s.

85 Extracted cardiac cycle lengths vary for each cardiac cycle and each measurement. The patient is known
86 to have an existing aneurysm in the MCA on the opposite (left) side, within which the velocity magnitudes
87 could not be clearly resolved using TCD due to its unfavourable orientation. We segmented the images
88 using VMTKlab (vmtklab.robix.com), and voxelized the 3D model using the HemeLB setup tool (see Fig.
89 1b). The resulting geometry has one inflow region and five outflow regions - two small ones at the top near
90 the inflow boundary, two larger ones at the bottom, and the largest one left of the 49 mm plane.

91 The 2D inflow profiles were reconstructed from the 1D TCD data by mapping a parabolic profile to the
92 non-circular inlets. This parabolic inlet profile has the original velocity from the 1D TCD data mapped
93 to the centre of the inlet (the lattice site which is furthest from any wall), and 0 velocity values mapped
94 to wall boundary sites. The velocity magnitude of a given lattice site is then calculated using a parabolic
95 equation, which depends on the distance of the lattice site to the nearest vessel wall site in the inlet plane (0
96 for wall sites, 1 for the site in the centre, and values in between for other sites).

97 The boundary conditions in the lattice Boltzmann method were implemented as follows. To set the
98 reconstructed velocity profile $\vec{u}_{\text{TCD}}(\vec{x}_{\text{in}}, t)$ at the inlet, we use a method introduced by Ladd (27). A simple
99 bounce-back boundary condition is augmented with a momentum term that results in a time-dependent

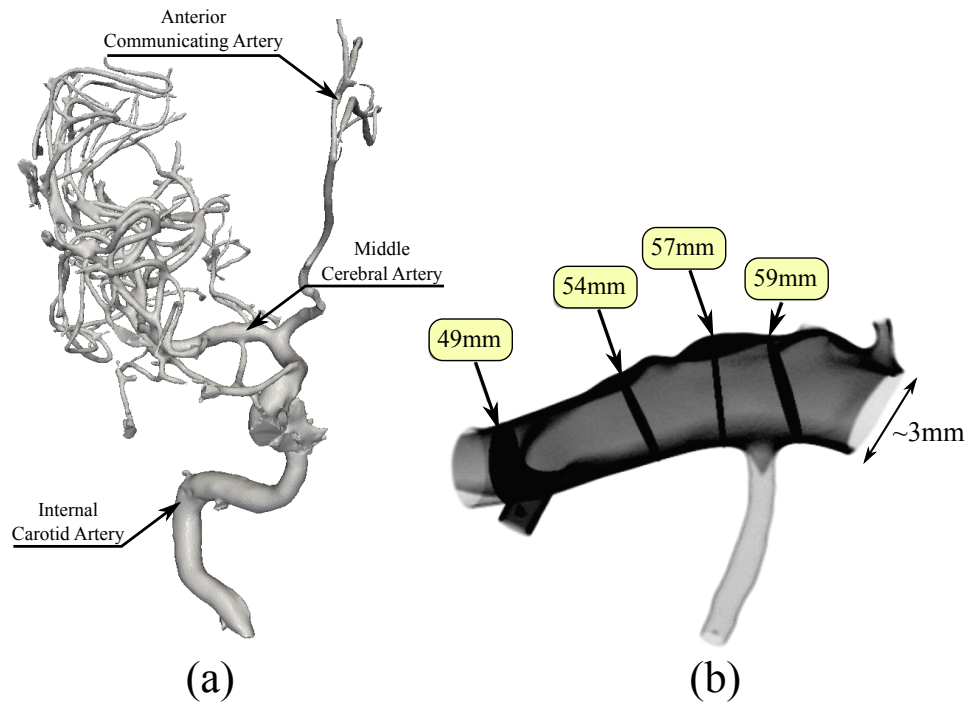


Figure 1. Overview of the overall patient vasculature in the medical images (a), and the patient-specific 3D model used in our simulations (b). As part of the simulation model overview, we indicate the four TCD measurement planes used for validation. Both the inlet and the 63 mm TCD measurement plane are at the right hand side of the image.

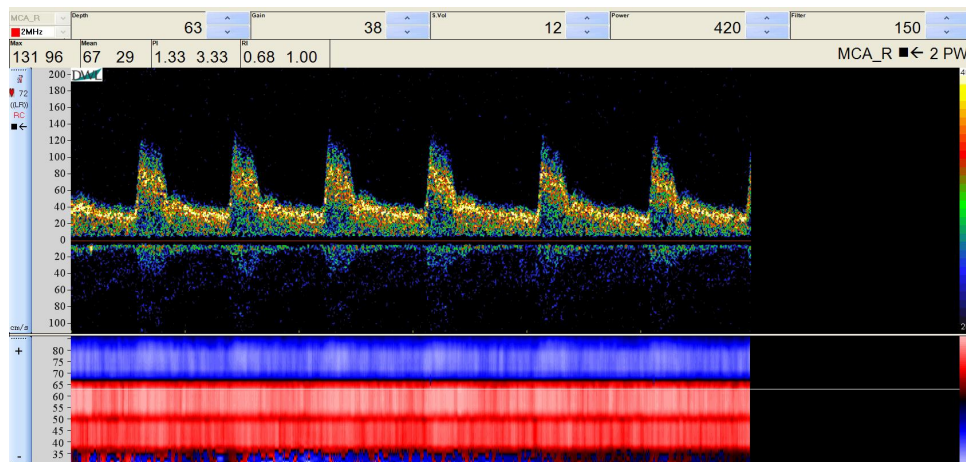


Figure 2. Raw TCD input image of the measured velocity at a depth of 63 mm (inflow boundary plane). The measured velocity at the selected depth (63 mm) is given at the top, while the general flow direction at all depths is given at the bottom, either towards the device (red) or away from it (blue). We observe a change in flow direction around a depth of 67 mm, which is at the junction between the right MCA and the right ACA.

100 Dirichlet condition for the velocity

$$\vec{u}(\vec{x}_{\text{in}}, t) = \vec{u}_{\text{TCD}}(\vec{x}_{\text{in}}, t). \quad (1)$$

	Distance from TCD device	Location (4 d.p.)	Normal (4 d.p.)
Triangulation point 1	45mm	[35.5,-203.8,-154.658]	-
Triangulation point 2	50mm	[22.3,-209.8,-156]	-
Triangulation point 3	66mm	[35.3,-203.8,-154.658]	-
Measurement plane 1	49mm	[21,-210.2,-156.5]	[0.9474,0.2650,0.1796]
Measurement plane 2	54mm	[25.4,-207.8,-154.9]	[0.6700,0.6437,0.3699]
Measurement plane 3	57mm	[27.5,-205.8,-154]	[0.8412,0.5309,0.1031]
Measurement plane 4	59mm	[29.6,-204.5,-154]	[0.7632,0.6017,0.2357]
Input plane	63mm	[32.6847,-203.4475,-154.6588]	[-0.9440,-0.0722,0.3220]
Output plane 1	-	[0.0316,-0.2009,-0.1520]	[0.2656,0.0262,-0.9637]
Output plane 2	-	[0.0298,-0.2102,-0.1618]	[-0.0834,0.8633,0.4977]
Output plane 2	-	[0.0240,-0.2143,-0.1570]	[0.1206,0.6726,0.7301]
Output plane 2	-	[0.0196,-0.2107,-0.1569]	[0.9685,0.2220,0.1124]

Table 1. Triangulation points, input, output and measurement plane locations (and orientations where applicable) in the simulation domain, used to calculate the angle correction.

At the outlet, we employed an open boundary condition in terms of a mixed Dirichlet-Neumann boundary condition (24)

$$\vec{u}_p(\vec{x}_{\text{out}}, t) = 0, \quad (2)$$

$$\hat{n} \cdot \nabla \vec{u}_n(\vec{x}_{\text{out}}, t) = 0, \quad (3)$$

101 where \hat{n} is the normal vector of the outlet plane, and \vec{u}_p and \vec{u}_n are the in-plane and normal components
 102 of the outlet velocity, respectively. The gradient in Eq. 3 is taken as the first-order finite difference
 103 approximation on the lattice Boltzmann grid. In the implementation by Nash et al. (24), the density
 104 $\rho(\vec{x}_{\text{out}}, t) = \rho_0$ at the outlet is prescribed in order to determine the unknown fluid variables. It is worth
 105 noting that prescribing the density at the outlet fixes the static pressure through the ideal gas equation of
 106 state. However, this does not constrain the dynamic pressure which varies over a cardiac cycle as shown in
 107 Figure 3.

108 The shear-thinning behaviour of blood is modeled using the Carreau-Yasuda (CY) model which employs
 109 the expression (28, 7)

$$\frac{\eta(\dot{\gamma}) - \eta_{\infty}}{\eta_0 - \eta_{\infty}} = (1 + (\lambda\dot{\gamma})^a)^{\frac{n-1}{a}} \quad (4)$$

110 to account for the dependence of the dynamic viscosity η on the shear rate $\dot{\gamma}$. Here, η_0 and η_{∞} are the
 111 asymptotic values at zero and infinite shear rate, and a , n , λ are empirical materials parameters that describe
 112 the shear-thinning curve. The CY model represents a smooth transition between Newtonian behavior at η_0
 113 and η_{∞} .

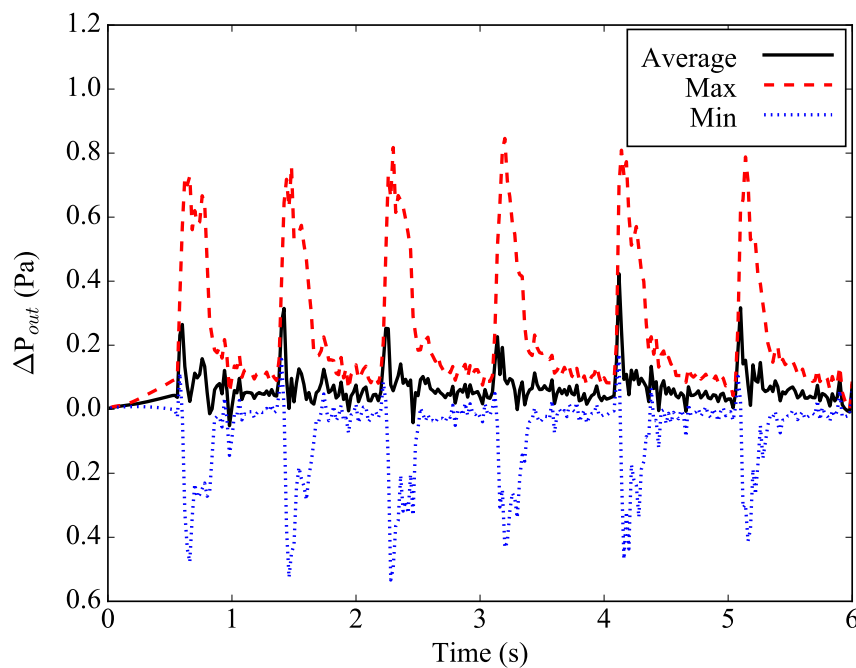


Figure 3. Differential pressure at the main outlet plane, relative to the ideal gas pressure for average density in the simulation. The maximal pressure found in the plane is given by the red dashed line, while the minimal pressure found in the plane is given by the blue dotted line. The average pressure in the plane is given by the black line.

114 The HemeLB simulations were performed on the ARCHER supercomputer at EPCC in Edinburgh,
 115 United Kingdom, and the SuperMUC supercomputer at LRZ in Garching, Germany. We used between
 116 1,536 and 24,768 cores, depending on the chosen resolution.

117 2.1 Choice of lattice Boltzmann parameters

118 Our lattice Boltzmann model uses a D3Q19 lattice with the Lattice Bhatnagar–Gross–Krook (LBGK)
 119 collision model (29). The relaxation parameters are set to yield the dynamic viscosity of blood of $\eta=0.004$
 120 Pa·s. The parameters used in the CY model are $\eta_0=0.16$ Pa·s, $\eta_\infty=0.0035$ Pa·s, $\lambda=8.2$ s, $a=0.64$ and
 121 $n=0.2128$ as given by Boyd et al. (28) and previously adopted by Bernabeu et al. (7). In our full-resolution,
 122 full-velocity simulations, we used a voxel size of $10\ \mu\text{m}$, a time step size of $0.28\ \mu\text{s}$, and a geometry
 123 consisting of 174,738,326 fluid sites. The simulations ran for 21.43 million time steps, which corresponds
 124 to five seconds of simulated time following a one-second “warmup” period (during which the inlet flow
 125 speed is increased gradually from rest in order to avoid flow instability or shockwaves resulting from
 126 a step change). The Reynolds number of our full-velocity simulation is approximately 966, based on a
 127 characteristic diameter of 24 mm with the highest measured peak velocity of 1.61 m/s.

128 We also performed simulations at reduced velocity and resolution, multiplying the velocities by 50% or
 129 25%, as well as with increased voxel sizes of $20\ \mu\text{m}$ and $40\ \mu\text{m}$. We discuss the implications of using this
 130 type of velocity scaling in detail in the next subsection.

131 **2.2 Velocity scaling**

The LBM is valid in the incompressible regime and introduces compressibility errors that scale quadratically in the Mach number $Ma = U/c_s$, where U is the flow velocity and c_s the speed of sound. The cardiac flow is characterized by the Reynolds number $Re = UD/\nu$ and the Womersley number $\alpha = (\omega D^2/\nu)^{1/2}$, where D is the vessel diameter, $\nu = \eta/\rho$ is the kinematic viscosity, and ω is the angular frequency of the oscillating flow due to the cardiac cycle. In terms of the simulation parameters, the kinematic viscosity of the lattice BGK model and the speed of sound are given by

$$\nu = \frac{1}{3} \left(\hat{\tau} - \frac{1}{2} \right) \frac{(\Delta x)^2}{\Delta t}, \quad (5)$$

$$c_s = \frac{1}{\sqrt{3}} \frac{\Delta x}{\Delta t}, \quad (6)$$

132 where $\hat{\tau}$ is the dimensionless relaxation parameter of the BGK model, and Δx and Δt are the discrete lattice
133 spacing and time step, respectively. Based on the Reynolds and Mach numbers, we have the following
134 relation for the dimensionless relaxation parameter

$$\hat{\tau} - \frac{1}{2} = \sqrt{3} \frac{D}{\Delta x} \frac{Ma}{Re}. \quad (7)$$

135 Linear stability requires $\hat{\tau} > 0.5$ which guarantees a positive viscosity. However, it is mandatory to
136 keep the Mach number small in order to reduce compressibility errors and make the system less prone
137 to instabilities due to density fluctuations. In the standard diffusive scaling, convergence is achieved by
138 reducing the Mach number while keeping the Reynolds number constant. This implies $(\Delta x)^2 \sim \Delta t$. Thus,
139 reducing the Mach number by means of increasing resolution results in an increase in computational costs
140 due to the cubic scaling of volume.

141 Therefore, some authors have been tempted to use lower flow velocities, e.g., from healthy subjects (1, 2),
142 in order to maintain stable simulations at a larger voxel size Δx . The ratio of the reduced velocity U' and
143 the original velocity U is denoted by a scaling factor s . This leads to a scaling relation

$$s = \frac{U'}{U} = \frac{\nu' Re' D}{\nu Re D'} = \frac{\alpha'^2 \omega' D' Re'}{\alpha^2 \omega D Re}, \quad (8)$$

144 where the prime denotes the quantities associated with the scaled velocity U' . If one insists on a fixed
145 system size $D' = D$ and cardiac cycle length $\omega' = \omega$, it is not possible to fix both the Womersley number
146 and the Reynolds number at the same time such that the simulation is performed in a flow regime different
147 to that of the full velocity simulation. In section 3.2, we demonstrate that this can significantly impact the
148 simulated flow patterns.

3 RESULTS AND DISCUSSION

149 We present results from three types of simulation. First, we compare our full velocity and full resolution
150 (10 micron voxel size) simulations against the TCD measurements on the same patient. Second, we present
151 the results from simulations at reduced velocity and reduced resolution, and compare them both with
152 results from our full-scale simulations and with the TCD measurements. Third, we compare the results of

Depth [mm]	49	54	57	59	63 (inflow)
Mean cycle length [s]	0.930	0.786	0.906	0.804	0.894
Maximum cycle length [s]	0.972	0.822	0.972	0.822	0.978
Minimum cycle length [s]	0.870	0.708	0.828	0.786	0.816
v_{\max}^{TCD} [m/s]	1.43	1.61	1.32	1.26	1.50
$v_{\max}^{\text{sim,Newton}}$ [m/s]	1.32	1.50	1.27	1.37	1.50*
d_r^{Newton}	-7.7%	-6.8%	-3.8%	+8.7%	-
$v_{\max}^{\text{sim,CY}}$ [m/s]	1.32	1.51	1.27	1.37	1.50*
d_r^{CY}	-7.7%	-6.2%	-3.8%	+8.7%	-

Table 2. Overview of measured and simulated flow characteristics in the MCA, as well as relative differences between measurement and simulation. In rows 1,2 and 3 we report the mean, maximum and minimum cardiac cycle length extracted from the TCD velocity measurements, respectively. In row 4 we provide the maximum velocity (v_{\max}) as measured in the TCD data, and in rows 5 and 7 we present v_{\max} for our (full velocity) HemeLB simulations with the Newtonian and the CY rheology models, respectively. Relative differences (d_r) between the TCD measurements and each of the respective two HemeLB simulations are in rows 6 and 8. We use the velocity as obtained from TCD as the inflow condition for our simulation.

153 simulations using a Newtonian rheology model to simulations using a non-Newtonian (Carreau-Yasuda)
 154 rheology model (30).

155 3.1 Validating full velocity haemodynamics predictions against measurements

156 In Table 2 we present the maximum velocity v_{\max} as measured with TCD and the simulation results for
 157 all four measurement planes. Our simulations predict the flow velocity with a relative error of less than
 158 9% in all cases. In Fig. 4 we present a direct comparison of our TCD measurements in the four planes
 159 over time, and our velocity predictions derived using HemeLB at the same locations. We observe good
 160 agreement between the simulation results and the measured TCD profile. The differences can be ascribed
 161 to the limitations of our approach (see Section 3.4) and uncertainties in the measurements, including phase
 162 misalignments due to the sequential nature of the TCD measurement.

163 In Fig. 5a-d, we present the two-dimensional velocity profiles extracted from the simulation at the four
 164 measurements planes. These profiles were extracted at the peak systole of the second cycle, corresponding
 165 to a velocity at the inlet of approximately 1.42 m/s. The figures show how the profile changes along the flow
 166 through the MCA. Compared to the inflow profile, the velocity profile at 59 mm is already substantially
 167 different, as a high velocity region is visible on the left side of the artery. The profiles at 57 and 54 mm
 168 show a strong concentration of velocity near the top, which is presumably due to the bend present in that
 169 region of the artery, while a bend in the opposite direction just before the 49 mm plane is the likely cause
 170 of the more evenly distributed velocities there at peak systole (Fig. 5e). In Fig. 5e-f we show the calculated
 171 wall shear stress (WSS) across the MCA at peak systole and diastole (at 2.18s). The front in Fig. 5e-f
 172 corresponds to the left side in Fig. 5a-d. We observe a WSS of >40 Pa during the systole in at least three
 173 locations. The WSS at the subsequent diastole (Fig. 5f) remains relatively high at the location near the
 174 second outlet at the top, which indicates that this location could be susceptible to the formation of a new
 175 aneurysm.

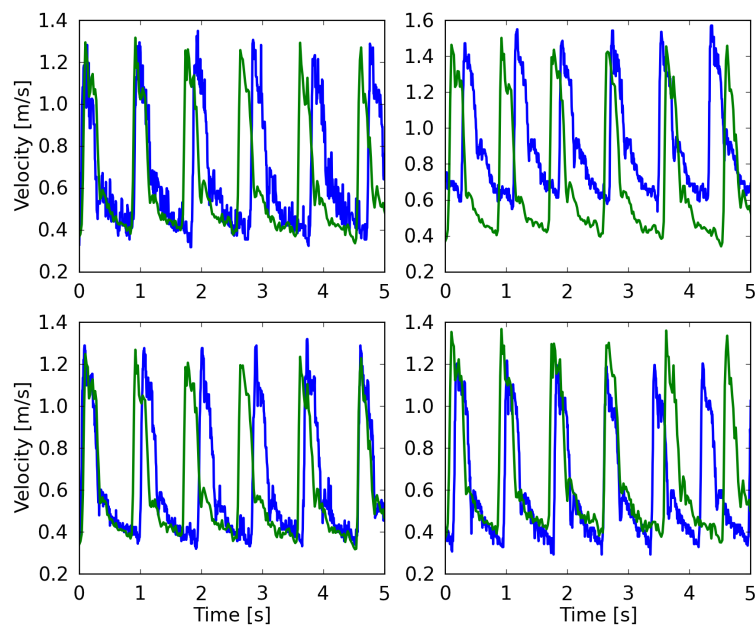


Figure 4. Comparison of the maximum velocity using both TCD (blue line) HemeLB (green line), given for the planes at 49 mm (top left), 54 mm (top right), 57 mm (bottom left) and 59 mm (bottom right). HemeLB results presented here are for the run at 100% velocity and with Newtonian rheology. The phase has been shifted to align both results with the start of the first cardiac cycle.

176 3.2 Full versus reduced velocity simulations

177 In this section we compare the velocity profiles at peak systole from simulations at 10 μm voxel size and
 178 full velocity with those at reduced velocity and/or increased voxel size. Reduced velocity and resolution
 179 runs are attractive because they are cheaper, faster to run and more likely to become computationally
 180 tractable in a clinical setting. For example, at time of writing a full velocity run across five cardiac cycles
 181 costs approximately £4200 on the ARCHER supercomputer (31), whereas a run at 50% velocity and
 182 the same resolution costs £2100 and a run at 50% velocity and 20 μm voxel size costs £500 to perform.
 183 However, reduced velocity simulations have a lower Reynolds number which affects a wide range of flow
 184 properties. In this study we have performed runs at 50% velocity ($\text{Re} \sim 483$) and 25% velocity ($\text{Re} \sim 242$).

185 We compare our simulation results at full velocity and resolution with those at reduced velocity and
 186 resolution in Fig. 6, and Table 3. When we reduce the inflow velocity by 50%, the maximum inflow velocity
 187 at the inlet is 0.75 m/s (not an uncommon value for healthy volunteers) (32) instead of 1.50 m/s (not an
 188 uncommon value for stroke patients (33)). We multiply the extracted velocities from our reduced velocity
 189 runs by two for simulations at 50% inflow velocity, and by four for simulations at 25% velocity. When
 190 comparing the runs with full inflow velocity runs with those at 50%, we already observe major differences
 191 in the extracted velocities. Here the comparisons at all four locations feature velocity differences of more
 192 than 0.4 m/s, and more than 30% of the maximum absolute flow velocity extracted in the corresponding
 193 plane. For the planes at 49 and 57 mm we see very large velocity differences near the vessel wall. This is
 194 likely due to the much higher Reynolds number of the flow in the full velocity run. When we compare the
 195 rescaled 50% velocity runs to the TCD measurements, the velocities differ by up to 15.5%, which is almost
 196 twice as large as the 8.8% maximum difference between TCD measurements and full velocity runs.

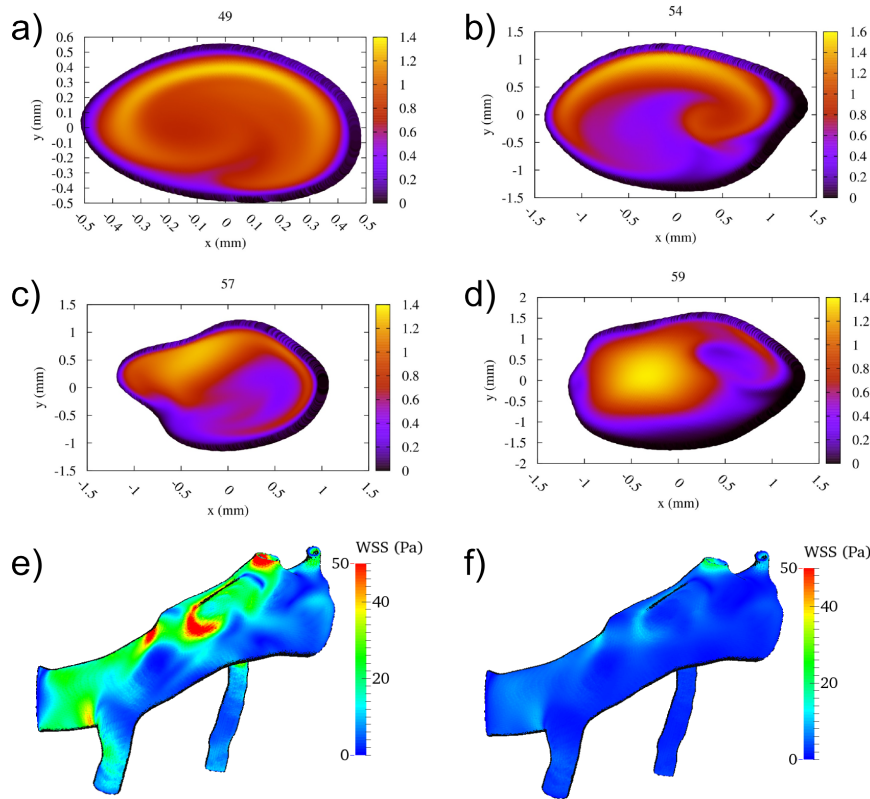


Figure 5. Calculated flow velocity magnitude, in the direction along the vessel centre lines, at the second peak systole (at 1.44s) in m/s for each of the four TCD validation planes. We show the velocity profiles in panels (a)-(d) for planes at a depth at 49, 54, 57 and 59mm respectively (run at 100% velocity, Newtonian rheology). We present the calculated wall shear stress (WSS) at peak systole in panel (e), and at diastole (at 2.18s) in panel (f) (using the same scale).

v scaling %	rheology	voxel size [μm]	$v_{\text{max}}^{\text{sim}}$ at depth [mm]				d_r [%] at depth [mm]			
			49	54	57	59	49	54	57	59
100%	Newton	10	1.32	1.50	1.27	1.37	-7.7	-6.8	-3.8	+8.7
100%	CY	10	1.32	1.51	1.27	1.37	-7.7	-6.2	-3.8	+8.7
50%	Newton	10	1.26	1.36	1.22	1.34	-11.9	-15.5	-7.6	+6.3
50%	Newton	20	1.25	1.36	1.22	1.34	-12.6	-15.5	-7.6	+6.3
50%	CY	20	1.25	1.36	1.22	1.34	-12.6	-15.5	-7.6	+6.3
25%	Newton	20	1.26	1.22	1.15	1.27	-11.9	-24.2	-12.9	+0.8
TCD measurement			1.43	1.61	1.32	1.26	-	-	-	-

Table 3. Comparison of full and reduced velocity simulations against TCD velocity measurements. We present the velocity scaling used in each run in column 1 (100% for a full velocity run), the rheology model used in column 2, the voxel size used in column 3 (10 μm for a full resolution run), the extracted peak velocity in each of the measurement planes in columns 4 to 7, and the relative difference in peak velocity compared to TCD measurements for each plane in columns 8 to 11. As a reference, we provide $v_{\text{max}}^{\text{TCD}}$ for each of the planes in the bottom row.

197 The results of the 50% velocity run with 20 μm voxel size are almost identical to the one with 10 μm
 198 voxel size, with only very small differences in all the velocity planes. However, the run with 25% velocity

199 is considerably less accurate, with absolute velocity differences up to 0.75 m/s, in particular close to the
 200 vessel walls. These errors are still smaller close to the inflow boundary at 59 mm, but dominate the overall
 201 result in the validation planes that are beyond the bifurcation with lenticulostriate arteries.

202 We conclude that simulations with reduced velocities affect the accuracy of the results significantly. This
 203 is particularly important because realistic velocities close to the wall are essential to obtain accurate wall
 204 shear stress estimates. We find that no such estimates can be reliably made for half velocity runs.

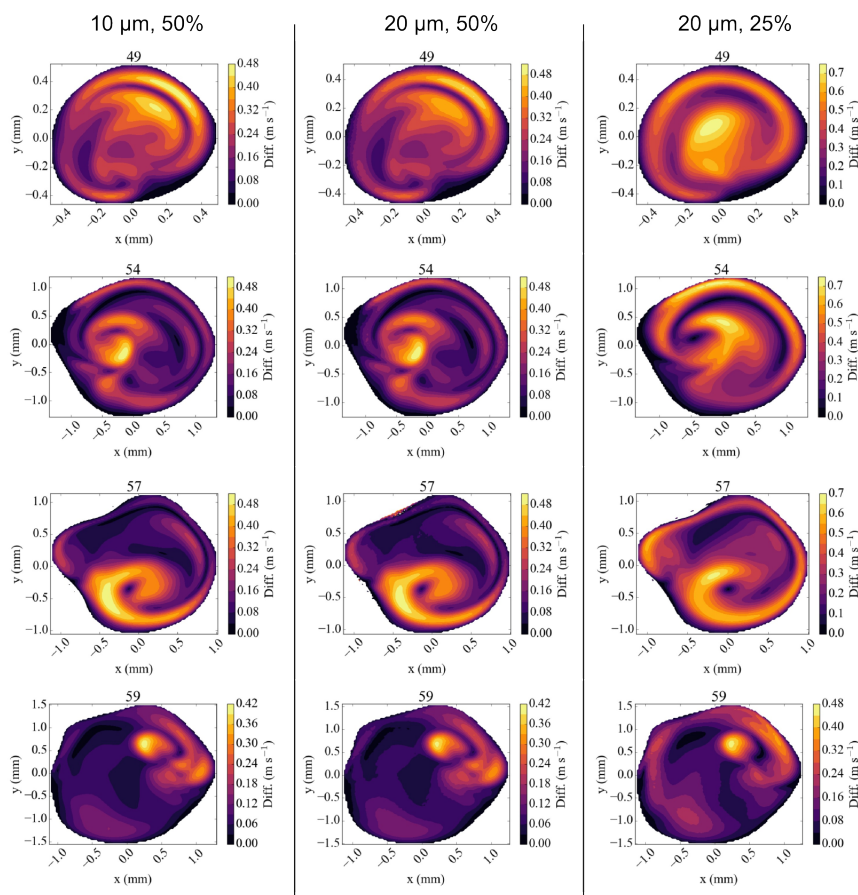


Figure 6. Absolute difference in flow velocity, between the run with Newtonian rheology at 10 micron resolution and 100% velocity and other runs for each of the four validation planes. Comparisons are made with runs at 10 μm and 50% velocity (left column), 20 μm and 50% velocity (middle), and 20 μm and 25% velocity (right) respectively. The velocities in reduced velocity runs are multiplied by 2 (for the 50% velocity runs) or 4 (for the 25% velocity runs). The snapshots were made at the second peak systole (at 1.44s), with differences in m/s.

205 3.3 Comparing rheology models

206 To compare different rheology models, we performed simulations on our MCA geometry using a Carreau-
 207 Yasuda (CY) rheology model (30). When the CY model was adopted, Bernabeu et al. found important
 208 differences in the WSS and Three-Band-Diagram analysis outcome for the MCA under “healthy human”
 209 flow conditions. Here we focus on differences in velocities obtained from the two rheology models, as we
 210 are interested in comparing simulation predictions to TCD measurements.

211 The difference in flow velocity between the Newtonian rheology model and the CY rheology model at
 212 peak systole is shown in Fig. 7. We observe differences in velocity of up to 0.12 m/s in three of the four

213 validation planes, and a difference of up to 0.21 m/s in a highly concentrated central region in the 54 mm
 214 measurement plane. In all cases the velocity differences are largest in regions where the absolute velocity
 215 is relatively small in the Newtonian rheology results, cf. Fig. 5, while only smaller differences exist in
 216 regions where the velocity is relatively large. These results suggest that the choice of using either a CY or
 217 Newtonian rheology model has little effect on v_{\max}^{sim} in all our comparisons (see Table 3).

218 The difference between the Newtonian and the CY rheology model for 50% reduced velocity is shown in
 219 Fig. 8 at peak systole. As noted above, velocity extractions from runs at 50% velocity are multiplied by 2
 220 to enable a direct comparison with full velocity runs. The difference in velocities between the 50% runs is
 221 considerably smaller than for 100% velocity runs, reaching at most 0.05 m/s in any of the measurement
 222 planes. The velocity difference is largest close to the arterial wall, but is in all cases much smaller than
 223 the velocity mismatch introduced by the velocity reduction (see Fig. 6, left row). This is in line with the
 224 finding that the choice of the rheology model has a small effect, and in the reduced velocity runs the impact
 225 of scaling down the velocity on accuracy is the dominating factor.

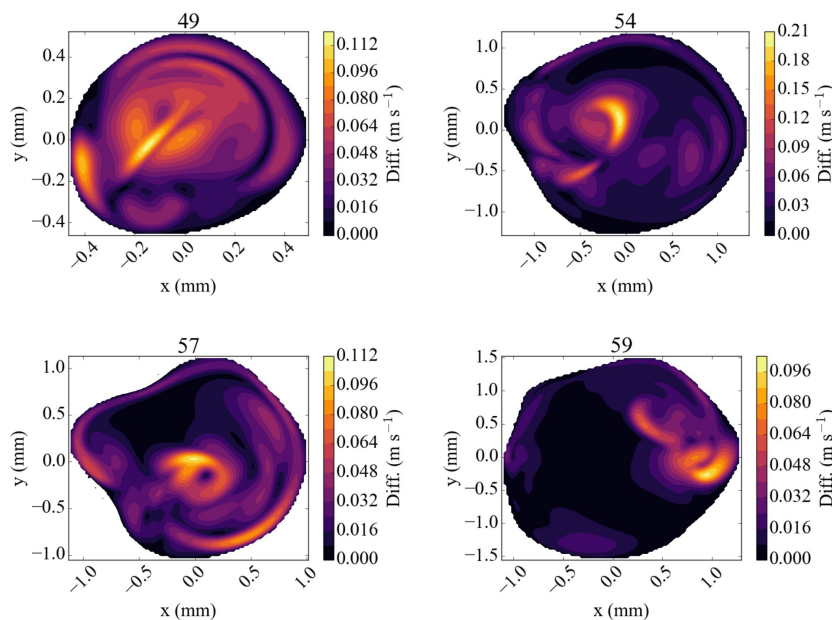


Figure 7. Absolute difference in flow velocity, between the run with Newtonian rheology and run with CY rheology. Both of these runs were performed at 100% of the full velocity. The snapshots were made at the second peak systole (at 1.44s), with differences in m/s, for each of the four TCD validation planes.

226 3.4 Limitations of our study

227 The main limitations of our validation study are related to data acquisition, model construction and
 228 simulation constraints.

229 Regarding TCD measurements, phase misalignments are common when directly comparing simulation
 230 results to these measurements, due to differences in apparent cardiac cycle length between the consecutively
 231 measured TCD planes (see Fig. 4). Furthermore, due to the proprietary nature of the TCD numerical data,
 232 numerical velocity values were extracted semi-automatically from JPEG images obtained with the Doppler
 233 BoxX software, which may introduce small measurement errors of up to 0.0064 m/s due to the resolution of

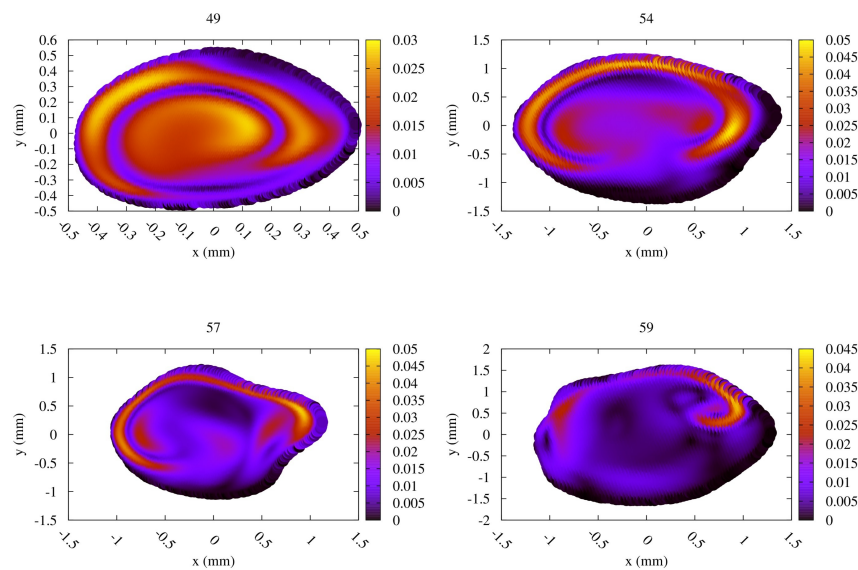


Figure 8. Absolute difference in flow velocity, between the run with Newtonian rheology and run with CY rheology. Both of these runs were performed at 50% of the full velocity, with the differences rescaled by a factor 2. The snapshots were made at the second peak systole (at 1.44s), with differences in m/s, for each of the four TCD validation planes.

234 the images. the measurement quality and level of background noise can vary with different measurements,
 235 as different depths are subject to varying levels of occlusion and wave propagation interference.

236 In the area of segmentation it is particularly challenging to accurately reproduce the small lenticulostriate
 237 arteries originating near the origin of the MCA (34). These arteries are not always clearly captured in
 238 the medical imaging data, and many existing haemodynamics models of MCAs do not include them,
 239 while our geometry contains two of these arteries. However, omitting them altogether can lead to velocity
 240 overestimations in the remainder of the MCA. In our model we were able to resolve the lenticulostriate
 241 arteries to a limited extent after extensive segmentation efforts.

242 Due to the one-dimensional nature of the TCD measurement, we used a parabolic inflow velocity profile
 243 and fitted it to the non-circular shapes of the inflow boundaries (see Sec. 2). Real inflow velocity profiles
 244 can vary depending on the morphology of the arterial network, as shown for example by Takeuchi and
 245 Takeshi (35). Regarding the outlets, a more physiologically accurate choice of boundary condition would
 246 take into account the downstream peripheral resistance. However, such an approach introduces additional
 247 patient-specific parameters. For the purposes of the validation conducted in this study we intentionally
 248 limit the complexity of the model and thus use a simple mixed Neumann-Dirichlet boundary condition.

249 Furthermore, our simulation model is based on a rigid geometry and does not include elastic deformations
 250 of the vessel. In case of blood flow in cerebral aneurysms, Dempere-Marco et al. (36) found that incorpor-
 251 ating wall motion has relatively little effect on the WSS. Understanding the dynamical response of arterial
 252 walls in the MCA, on a patient-specific level, is a particularly challenging area of research. However, recent
 253 studies show promising results that should soon allow us to examine these processes (37, 38).

254 3.5 Future work

255 There are a range of factors that we seek to incorporate in our model as part of our future research.
256 Firstly, we aim to develop techniques to create more realistic inflow profiles by using simulation data
257 of arteries upstream from the patient's MCA. Secondly, we seek to enhance our model by incorporating
258 mechanisms for arterial wall deformations and damage. Such mechanisms are highly complex and very
259 difficult to measure experimentally, and therefore modelling them is a particularly challenging area of
260 research. Thirdly, we seek to provide more realistic outflow properties by extending our geometry to
261 arteries further downstream. This could be accomplished for example by investigating how existing (1D)
262 resistance models could be accurately applied within the context of complex 3D simulation models, or by
263 attempting to simulate the full human brain in 3D over realistic time scales, and using patient-specific flow
264 conditions.

4 CONCLUSIONS

265 We have conducted a validation study comparing flow velocities from patient-specific lattice-Boltzmann
266 simulations to clinical TCD measurements in the MCA. As part of the study, we analyzed simulation
267 results obtained at reduced velocities and variable resolution. Moreover, we investigated the impact of
268 using the Carrueau-Yasuda rheology model compared to a Newtonian rheology model.

269 We achieved very good agreement of the maximum velocity between our full patient-specific velocity
270 simulation results and TCD measurements, with an error of less than 9% independent of the choice of
271 rheology model. Simulating blood flow at reduced velocities, for example by scaling down the velocity
272 or using velocity measurements from healthy subjects, is attractive because the simulation runs are
273 computationally cheaper and deliver results faster. However, we found that scaling down the flow velocities
274 leads to substantially larger errors, and an accurate comparison between simulations and TCD measurements
275 is no longer achieved. Adopting a CY rheology model instead of a Newtonian one results in small changes
276 in maximum velocities in the planes and in our validation, whereas substantial flow velocity differences
277 are observed near the arterial wall and in the resulting WSS. However, the CY rheology model does not
278 enable a significant improvement when the velocity is already scaled down (e.g., by using inflow profiles
279 of healthy volunteers or reduced velocity Womersley profiles), as errors caused by this velocity scaling
280 then dominate the overall accuracy. Figures 7 and 8 suggest that a Newtonian rheology model may be a
281 justifiable approximation for MCA simulations at lower (i.e. < 0.75 m/s) peak flow, but that this could
282 quickly become problematic for the higher flows typically recorded in unhealthy patients (in which 1.5 m/s
283 is not unusual).

284 Computational haemodynamics predictions that accurately match patient-specific TCD measurements
285 are likely to become an important asset in clinical settings and pave the way to using computer models in
286 the process of clinical decision making (39, 40). Compared to clinical measurements alone, patient-specific
287 simulations allow us to obtain information about a much wider range of flow properties, such as detailed
288 flow velocity characteristics and wall shear stress estimates. In addition, simulations can help predict
289 flow velocity in areas that have not been directly measured, and thereby help reduce the number and
290 intensity of invasive measurements that need to be performed. Here we have shown that a combination
291 of non-invasive TCD measurements with haemodynamics simulations can lead to accurate predictions of
292 blood flow velocity throughout the MCA. The ability to make these accurate predictions constitutes an
293 important step in making computational haemodynamics a viable approach for assessing intracranial blood
294 flow.

CONFLICT OF INTEREST STATEMENT

295 The authors declare that the research was conducted in the absence of any commercial or financial
296 relationships that could be construed as a potential conflict of interest.

ETHICS STATEMENT

297 The patient-specific data (3D angiography, TCD measurements) used in this study was available “on the
298 shelf” and did not contain identifiable information. The segmented geometry is already published (21). The
299 present study involved only secondary analysis of de-identified data that is not linked to the subjects from
300 whom it was originally collected.

AUTHOR CONTRIBUTIONS

301 DG conceived the study, while DG and RR carried out the simulations, performed the validation comparison
302 and wrote the manuscript. US advised on the choice of simulation parameters and contributed to writing
303 the manuscript. RC segmented the medical images and extracted the TCD velocity profiles from the
304 measurement images, with help from DG, US, and PC. FR obtained the original angiography images, while
305 HC performed the TCD measurements. Both FR and HC advised on the medical aspects of the manuscript.
306 PC coordinated the study and helped draft the manuscript. All authors gave final approval for publication.

FUNDING

307 This work received funding from the EU FP7 CRESTA project (grant number, 287703), the EU H2020
308 projects ComPat (grant no. 671564) and CompBioMed (grant no. 675451), the EPSRC-funded 2020
309 Science Programme (EP/I017909/1), and the Qatar National Research Fund (NPRP), project No. 5-792-2-
310 238. RC is supported through doctoral training grant SP/08/004 from the British Heart Foundation (BHF),
311 through the UCL CoMPLEX doctoral training programme.

ACKNOWLEDGEMENTS

312 We thank Aditya Jitta for his efforts in analyzing a preliminary version of our MCA simulation model.
313 We are grateful to Rupert Nash, Miguel Bernabeu and Timm Krüger for useful discussions pertaining the
314 simulation parameters. We thank Ann Warner for her help in obtaining angiographic data, and Sebastian
315 Schmieschek in assisting with the supervision of RC. Access to the ARCHER supercomputer at EPCC
316 in the UK was provided by the UK Consortium on Mesoscopic Engineering Sciences (EP/L00030X/1).
317 In addition, we are grateful to the Leibniz Rechenzentrum (LRZ) in Germany for providing access to the
318 SuperMUC supercomputer.

SUPPLEMENTAL DATA

319 We provide the source data for our publication via Figshare under DOI:10.17633/rd.brunel.5001962. The
320 DOI will be activated upon acceptance of the manuscript, and we are happy to provide this data upon
321 request prior to that point.

REFERENCES

- 322 1 .Miura Y, Ishida F, Umeda Y, Tanemura H, Suzuki H, Matsushima S, et al. Low wall shear stress is
323 independently associated with the rupture status of middle cerebral artery aneurysms. *Stroke* **44** (2013)
324 519–521. doi:10.1161/STROKEAHA.112.675306.
- 325 2 .Byrne G, Mut F, Cebal J. Quantifying the large-scale hemodynamics of intracranial aneurysms.
326 *American Journal of Neuroradiology* **35** (2014) 333–338. doi:10.3174/ajnr.A3678.
- 327 3 .Mountrakis L, Lorenz E, Hoekstra AG. Where do the platelets go? a simulation study of fully resolved
328 blood flow through aneurysmal vessels. *Interface Focus* **3** (2013) 20120089. doi:10.1098/rsfs.2012.
329 0089.
- 330 4 .Ouared R, Larrabide I, Brina O, Bouillot P, Erceg G, Yilmaz H, et al. Computational fluid dynamics anal-
331 ysis of flow reduction induced by flow-diverting stents in intracranial aneurysms: a patient-unspecific
332 hemodynamics change perspective. *Journal of NeuroInterventional Surgery* **8** (2016) 1288–1293.
333 doi:10.1136/neurintsurg-2015-012154.
- 334 5 .Cebal JR, Mut F, Weir J, Putman C. Quantitative characterization of the hemodynamic environment in
335 ruptured and unruptured brain aneurysms. *American Journal of Neuroradiology* **32** (2011) 145–151.
- 336 6 .Xiang J, Tutino VM, Snyder KV, Meng H. CFD: computational fluid dynamics or confounding factor
337 dissemination? The role of hemodynamics in intracranial aneurysm rupture risk assessment. *American*
338 *Journal of Neuroradiology* **35** (2014) 1849–1857.
- 339 7 .Bernabeu MO, Nash RW, Groen D, Carver HB, Hetherington J, Krüger T, et al. Impact of blood
340 rheology on wall shear stress in a model of the middle cerebral artery. *J. R. Soc. Interface Focus* **3**
341 (2013). doi:10.1098/rsfs.2012.0094.
- 342 8 .Jou LD, Lee DH, Morsi H, Mawad ME. Wall shear stress on ruptured and unruptured intracranial
343 aneurysms at the internal carotid artery. *American Journal of Neuroradiology* **29** (2008) 1761–1767.
- 344 9 .Boussel L, Rayz V, McCulloch C, Martin A, Acevedo-Bolton G, Lawton M, et al. Aneurysm growth
345 occurs at region of low wall shear stress. *Stroke* **39** (2008) 2997–3002. doi:10.1161/STROKEAHA.
346 108.521617.
- 347 10 .Marzo P Aand Singh, Larrabide I, Radaelli A, Coley S, Gwilliam M, Wilkinson ID, et al. Computational
348 hemodynamics in cerebral aneurysms: The effects of modeled versus measured boundary conditions.
349 *Annals of Biomedical Engineering* **39** (2011) 884–896. doi:10.1007/s10439-010-0187-z.
- 350 11 .Hassan T, Ezura M, Timofeev EV, Tominaga T, Saito T, Takahashi A, et al. Computational simulation
351 of therapeutic parent artery occlusion to treat giant vertebrobasilar aneurysm. *American Journal of*
352 *Neuroradiology* **25** (2004) 63–68.
- 353 12 .Chang W, Landgraf B, Johnson KM, Kecskemeti S, Wu Y, Velikina J, et al. Velocity measurements in the
354 middle cerebral arteries of healthy volunteers using 3d radial phase-contrast HYPRFlow: Comparison
355 with transcranial Doppler sonography and 2d phase-contrast MR imaging. *American Journal of*
356 *Neuroradiology* **32** (2011) 54–59. doi:10.3174/ajnr.A2240.
- 357 13 .Meckel S, Leitner L, Bonati LH, Santini F, Schubert T, Stalder AF, et al. Intracranial artery velocity
358 measurement using 4D PC MRI at 3 T: comparison with transcranial ultrasound techniques and 2D PC
359 MRI. *Neuroradiology* **55** (2013) 389–398.
- 360 14 .Bernsdorf J, Wang D. Non-Newtonian blood flow simulation in cerebral aneurysms. *Computers &*
361 *Mathematics with Applications* **58** (2009) 1024–1029.
- 362 15 .Xiang J, Tremmel M, Kolega J, Levy EI, Natarajan SK, Meng H. Newtonian viscosity model could
363 overestimate wall shear stress in intracranial aneurysm domes and underestimate rupture risk. *Journal*
364 *of Neurointerventional Surgery* **4** (2011) 351–357.

- 365 **16** .Khan M, Steinman D, Valen-Sendstad K. Non-Newtonian versus numerical rheology: Practical impact
366 of shear-thinning on the prediction of stable and unstable flows in intracranial aneurysms. *International*
367 *Journal for Numerical Methods in Biomedical Engineering* (2016).
- 368 **17** .Chatzizisis YS, Jonas M, Coskun AU, Beigel R, Stone BV, Maynard C, et al. Prediction of the
369 localization of high-risk coronary atherosclerotic plaques on the basis of low endothelial shear stress.
370 *Circulation* **117** (2008) 993–1002.
- 371 **18** .Alnæs MS, Isaksen J, Mardal KA, Romner B, Morgan MK, Ingebrigtsen T. Computation of
372 hemodynamics in the circle of Willis. *Stroke* **38** (2007) 2500–2505.
- 373 **19** .Castro MA, Putman CM, Cebal JR. Computational fluid dynamics modeling of intracranial aneurysms:
374 effects of parent artery segmentation on intra-aneurysmal hemodynamics. *American Journal of*
375 *Neuroradiology* **27** (2006) 1703–1709.
- 376 **20** .Venugopal P, Valentino D, Schmitt H, Villablanca JP, Vinuela F, Duckwiler G. Sensitivity of patient-
377 specific numerical simulation of cerebral aneurysm hemodynamics to inflow boundary conditions.
378 *Journal of Neurosurgery* **106** (2007) 1051–1060. doi:10.3171/jns.2007.106.6.1051.
- 379 **21** .Itani MA, Schiller UD, Schmieschek S, Hetherington J, Bernabeu MO, Chandrashekar H, et al. An
380 automated multiscale ensemble simulation approach for vascular blood flow. *Journal of Computational*
381 *Science* **9** (2015) 150–155.
- 382 **22** .Jain K, Jiang J, Strother C, Mardal KA. Transitional hemodynamics in intracranial
383 aneurysms—comparative velocity investigations with high resolution lattice boltzmann simulations,
384 normal resolution ansys simulations, and MR imaging. *Medical Physics* **43** (2016) 6186–6198.
- 385 **23** .Groen D, Hetherington J, Carver HB, Nash RW, Bernabeu MO, Coveney PV. Analyzing and modeling
386 the performance of the HemeLB lattice-Boltzmann simulation environment. *Journal of Computational*
387 *Science* **4** (2013) 412 – 422.
- 388 **24** .Nash RW, Carver HB, Bernabeu MO, Hetherington J, Groen D, Krüger T, et al. Choice of boundary
389 condition for lattice-boltzmann simulation of moderate-Reynolds-number flow in complex domains.
390 *Phys. Rev. E* **89** (2014) 023303.
- 391 **25** .Succi S. *The Lattice Boltzmann Equation: For Fluid Dynamics and Beyond* (Oxford University Press)
392 (2001).
- 393 **26** .Bouzidi M, Firdaouss M, Lallemand P. Momentum transfer of a Boltzmann-lattice fluid with boundaries.
394 *Phys. Fluids* **13** (2001) 3452–3459. doi:10.1063/1.1399290.
- 395 **27** .Ladd AJC. Numerical simulations of particulate suspensions via a discretized Boltzmann equation.
396 Part 1. Theoretical foundation. *J. Fluid Mech.* **271** (1994) 285–309.
- 397 **28** .Boyd J, Buick JM, Green S. Analysis of the Casson and Carreau-Yasuda non-Newtonian blood models
398 in steady and oscillatory flows using the lattice Boltzmann method. *Physics of Fluids* **19** (2007) 093103.
- 399 **29** .Bhatnagar PL, Gross EP, Krook M. A model for collision processes in gases. I. Small amplitude
400 processes in charged and neutral one-component systems. *Phys. Rev.* **94** (1954) 511–525. doi:10.1103/
401 PhysRev.94.511.
- 402 **30** .Abraham F, Behr M, Heinkenschloss M. Shape optimization in steady blood flow: a numerical study
403 of non-newtonian effects. *Computer methods in biomechanics and biomedical engineering* **8** (2005)
404 127–137.
- 405 **31** .[Dataset] EPCC. ARCHER kAU Calculator (2017). <http://www.archer.ac.uk/access/au-calculator/>.
- 406 **32** .Bishop CC, Powell S, Rutt D, Browse NL. Transcranial Doppler measurement of middle cerebral
407 artery blood flow velocity: a validation study. *Stroke* **17** (1986) 913–915.

- 408 **33** .Manno EM, Gress DR, Schwamm LH, Diringer MN, Ogilvy CS. Effects of induced hypertension on
409 transcranial Doppler ultrasound velocities in patients after subarachnoid hemorrhage. *Stroke* **29** (1998)
410 422–428.
- 411 **34** .Kang CK, Woerz S, Liao W, Park CA, Kim YB, Park CW, et al. Three dimensional model-based analysis
412 of the lenticulostriate arteries and identification of the vessels correlated to the infarct area: Preliminary
413 results. *International Journal of Stroke* **7** (2012) 558–563. doi:10.1111/j.1747-4949.2011.00611.x.
- 414 **35** .Takeuchi S, Karino T. Flow patterns and distributions of fluid velocity and wall shear stress in the
415 human internal carotid and middle cerebral arteries. *World neurosurgery* **73** (2010) 174–185.
- 416 **36** .Dempere-Marco L, Oubel E, Castro M, Putman C, Frangi A, Cebal J. CFD analysis incorporating the
417 influence of wall motion: application to intracranial aneurysms. *International Conference on Medical
418 Image Computing and Computer-Assisted Intervention* (Springer) (2006), 438–445.
- 419 **37** .Vanrossomme AE, Eker OF, Thiran JP, Courbebaisse GP, Zouaoui Boudjeltia K. Intracranial aneurysms:
420 Wall motion analysis for prediction of rupture. *American Journal of Neuroradiology* **36** (2015)
421 1796–1802. doi:10.3174/ajnr.A4310.
- 422 **38** .Oubel E, Cebal J, De Craene M, Blanc R, Blasco J, Macho J, et al. Wall motion estimation in
423 intracranial aneurysms. *Physiological measurement* **31** (2010) 1119.
- 424 **39** .Sadiq SK, Mazzeo MD, Zasada SJ, Manos S, Stoica I, Gale CV, et al. Patient-specific simulation as a
425 basis for clinical decision-making. *Philosophical Transactions of the Royal Society A: Mathematical,
426 Physical and Engineering Sciences* **366** (2008) 3199–3219. doi:10.1098/rsta.2008.0100.
- 427 **40** .Fenner JW, Brook B, Clapworthy G, Coveney PV, Feipel V, Gregersen H, et al. The EuroPhysiome,
428 STEP and a roadmap for the virtual physiological human. *Philosophical Transactions of the Royal
429 Society of London A: Mathematical, Physical and Engineering Sciences* **366** (2008) 2979–2999.
430 doi:10.1098/rsta.2008.0089.